PHILOSOPHICAL TRANSACTIONS OF THE ROYAL SOCIETY A MATHEMATICAL, PHYSICAL & ENGINEERING SCIENCES

Porosity waves in a fluidized sand–column test

I. Vardoulakis, M. Stavropoulou and A. Skjaerstein

Phil. Trans. R. Soc. Lond. A 1998 **356**, 2591-2608
doi: 10.1098/rsta.1998.0288

THE ROYAL SOCIETY

Porosity waves in a fluidized sand-column test

By I. Vardoulakis[1], M. Stavropoulou[1] and A. Skjaerstein[2]

[1]*Department of Engineering Science, National Technical University of Athens, 5 Heroes of Polytechniou Avenue, GR-15773 Athens, Greece*

[2]*IKU, Norsk Hydro ASA, PB 200, 1321 Stabekk, Vaekero, Oslo, Norway*

Fluidized sand-column experiments performed at the IKU provided insight into the mechanism of density adjustment to the conditions of flow against the direction of gravity, and for hydraulic gradients around and past the critical value corresponding to the 'quick' condition. X-ray computer-tomography scan images obtained during these tests show a process which could be described as a kinematic density or porosity-wave motion. Forchheimer's flow law, holding in the post-critical regime, is calibrated by using the storage equation and the data concerning the propagation velocity of the observed porosity waves. Finally, the observed rarefaction waves are simulated mathematically and experimental results are back-analysed.

Keywords: fluidized sands; porosity waves; fluid flow; porous media

1. Introduction

The fluidized column experiment is used to study the phenomena of fluid-flow in granular media under relatively high hydraulic gradients, which act opposite to gravity. In the soil-mechanics literature, this test has been used extensively to analyse filtering processes and make assessments about the internal stability of the filter (cf. Kenney & Lau 1985). Notable is a recent paper by Skempton & Brogan (1994), who studied, experimentally, piping phenomena in internally unstable sandy gravels. Piping may be seen as an internal erosion process, which is due to the mobility of fines through the pores of coarser matrix, and can be modelled within the frame of a three-phase-mixture theory of solid, fluid and fines in transport (cf. Stavropoulou 1996; Vardoulakis *et al*. 1996).

In homodispersive media, internal mobility of grains is less probable, and other phenomena prevail. In papers by Kolymbas (1982, 1994) and Scott (1986*a*, *b*), the issue of density waves propagating in fluidized sands was addressed. In fluidized sand-column experiments performed recently at the IKU on uniform sands, fluid flow and density-wave propagation were monitored by using X-ray computer tomography (CT). In another paper by the authors (Skjaerstein *et al*. 1997) a three-phase-mixture model was proposed, which mainly addressed the issue of grain mobility. Here, the emphasis lies on the study of fluid flow under dynamic conditions in conjunction with porosity waves.

As is well known from soil-mechanics literature, at a critical hydraulic gradient J_{c}, the seepage force exerted on the grains by the flowing fluid in vertical flow balances their buoyant weight, and thus this critical hydraulic gradient has the value

$$J_{\mathrm{c}} = (1-\phi)\left(\frac{\rho_{\mathrm{s}}}{\rho_{\mathrm{f}}} - 1\right), \tag{1.1}$$

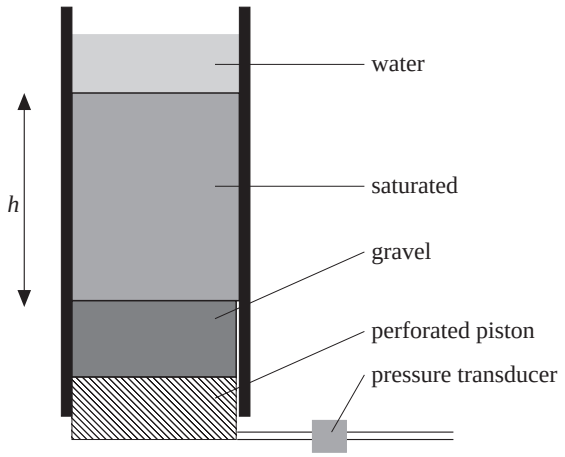

Figure 1. Schematic illustration of the set-up for the fluidized column experiment.

where ρ_s and ρ_f are the grain and fluid densities, respectively, and ϕ is the porosity of the mixture. At and past this critical hydraulic gradient, 'quicksand' conditions are holding, which are characterized by pronounced mobility of the sand due to loss of its strength. With increasing flow rate, there is a slow transition from purely laminar flow to mildly turbulent conditions. A rough criterion for the limit of applicability of Darcy's law for creeping flow is expressed in terms of the Reynolds number of the flow referred to the mean grain diameter, as $Re \leqslant 1$ (Taylor 1948). For higher Reynolds numbers, the relation between head-loss and discharge velocity is nonlinear. For one-dimensional flow with the discharge velocity q and hydraulic gradient J, Forchheimer (1914) suggested a polynomial expression

$$J = aq + bq^2, \tag{1.2}$$

where the first coefficient is usually identified with the hydraulic resistivity of the porous medium for laminar flow conditions. It should also be noted that, considering the Navier–Stokes equations for the fluid and flow passing through a periodic array of spherical grains, Irmay (1958) justified a more general form of Forchheimer's law, which included inertial effects as well. Irmay (1958) suggested particular expressions for the coefficients in the Forchheimer equation as functions of porosity and grain size (see Vardoulakis & Sulem 1995, § 5). These models are static, in the sense that during flow, porosity remains constant, and in most cases is considered homogeneous inside the tested sand column.

Due to pronounced internal grain mobility, quicksand behaves more like a fluid with the possibility of density fluctuations. This means that quicksand resembles a compressible fluid which is capable of carrying density waves. In this paper we readdress the issue of porosity waves earlier introduced by Kolymbas (1982, 1994) and Scott (1986*a*, *b*). This is done in conjunction with modelling of fluid flow in such a medium with variable density, consisting of water and homodispersive quicksand.

2. Experimental set-up and test results

The experimental set-up is illustrated in figure 1. The set-up consists of a perforated piston at the bottom and a cylindrical Plexiglas sleeve for visual observations of

deformations in the sand. The diameter of the sleeve is 100 mm. The sleeve is filled with a sequence of gravel, sand and water. Both the sand and the gravel are fully saturated when the test starts. Water flows through the bottom piston and is thereafter distributed by the gravel, before it flows axially upwards into the sand body. The gravel used has a mean grain size of 400–430 μm. The hydrostatic pressure measured at the inlet was taken as the 'zero' level and the flow rate was increased in steps. The flow rate was manually measured at the outlet, with an accuracy of ± 1 ml min^{-1}. The pressure was measured with an accuracy of ± 0.005 bar. The height of the sand column was measured from the X-ray CT scans, with an accuracy of ± 0.5 mm.

In addition to the visual observations, X-ray CT was used interactively to monitor sand-body deformation. The scanner is based on a rotating tube-detector system. The computer tomogram gives a matrix with a limited number of picture elements. The unit of the computer tomogram determines its spatial resolution. CT cross-sections were created with a 1 mm separation, and the resolution obtained was ($0.55 \times 0.55 \times 1$ mm^3). Each volume element has a numerical value representing the mean attenuation in the volume element. The material density value stands in a linear relationship to the attenuation coefficient. For each flow-rate level, several images were taken of the sample. These images showed density changes inside the sand-body due to variations of the fluid pressure gradient.

Two different types of sand were used in the fluidized-column experiments. The first one was a Danish beach sand with a mean grain size of about 160 μm; the second was called Valøygrind sand, which had a mean grain size of *ca.* 150 μm. The main difference between these two grain-size distributions is that the Danish beach sand does have a smaller grain-size spectrum. The beach sand exhibits a homogeneous grain size and shape (rounded), while the Valøygrind sand consists of angular and elongated grains. The grain-size distributions of the two sands are presented in figure 2. During the test, an equilibrium density and length of the sand column was reached for each flow rate. However, using the images, it was possible to obtain information about the process prior to equilibrium. The results from one test are given in terms of flow rate, dynamic inlet pressure, height of sand body, and 'CT-density' as functions of time. The 'CT-density' number is a number on the so-called Hounsfield scale, which is a linear function of the physical density.

The mean density of the sand body was calculated from the CT images. Density variations with time in the two tests on Danish beach sand and Valøygrind sand are presented in figure 3. From the plot it can be seen that the initial density is higher for Valøygrind sand than for Danish beach sand. The density of the sand body remains more or less constant up to a certain flow rate, after which it starts to decrease. This critical flow rate is lower in Valøygrind sand than in Danish beach sand. In this part of the test, the relationship between flow rate and density seems to be the same for the two sands. The density values presented could, in principle, be translated to real density values, but due to artefacts this would not give correct numbers.

Fluidized-column tests inside the CT scanner, as well as preliminary tests carried out with manual column-height measurements, showed that an equilibrium height was reached shortly after an increase in the flow rate. However, a significant transition regime between subsequent equilibria was experienced, and the test can consequently be divided into a transient and a steady-state regime. Figure 4 illustrates schematically the transient deformation of the sand body between two equilibrium flow rates.

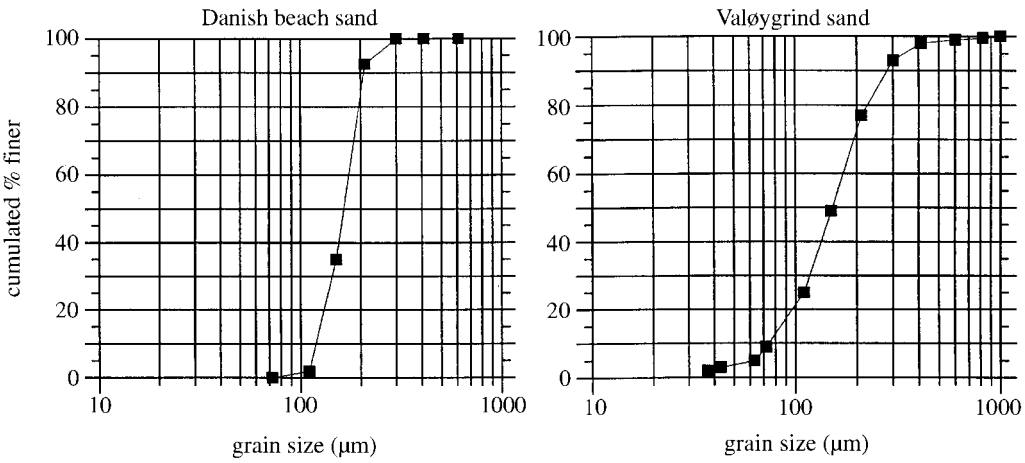

Figure 2. Grain-size distribution for Danish beach sand and Valøygrind sand.

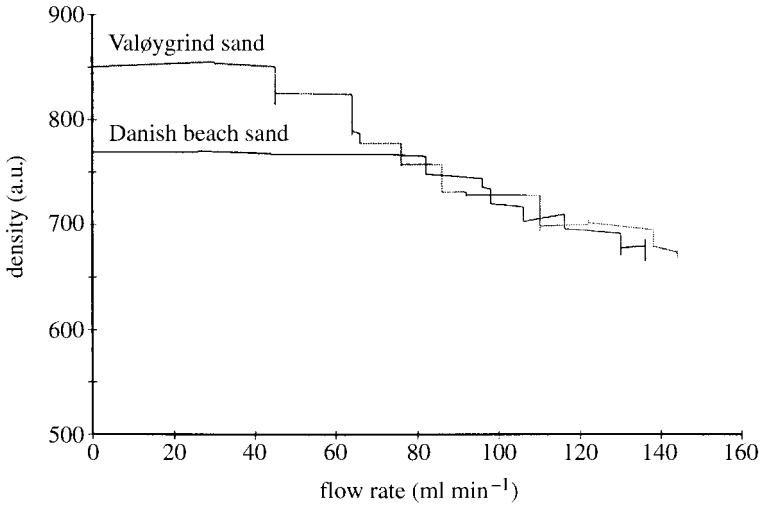

Figure 3. The density variations in the two fluidized-column tests.

CT images taken at constant flow rate in the transient regime illustrate the behaviour of the sand body. The images show a process that could be explained as a wave motion (see figure 5). A change in the flow rate gives rise to an upwards-propagating density wave in the sand body. When the wave reaches the top of the sand body a new equilibrium is reached. This wave motion was only observed for one flow rate change in the test on Danish beach sand, while the wave was seen for all flow rates in the Valøygrind sand. The reason for this difference was probably the relatively lower density contrast inside the sand body in the case of Danish beach sand as compared to the Valøygrind sand (possibly due to the differences in the grain-size distribution). An additional test was performed in Danish beach sand, where the flow rate was increased from zero to maximum in one step. In this test the density wave was observed. This test also confirmed that the amplitude of the density wave is related to the change in the flow rate. It is assumed that the density wave is appearing in the first test on Danish beach sand, but the density contrast is

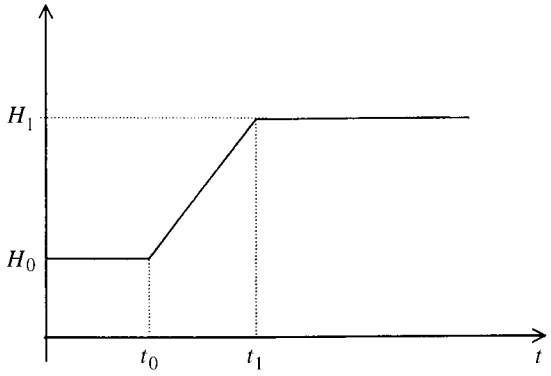

Figure 4. Schematic illustration of the height adjustment of the sand column due to increased fluid flow rate.

too small to be observed within the resolution of the scanner. The amplitude of the density wave is determined as the density difference between the wave front and the sand body. The density variations inside the sand body as a function of time were quantified for the second test on Danish beach sand by means of a mean-density value as a function of sand height. From the calculations, it was seen that the density is lower in the parts of the sample which the wave has passed through than in the remaining part of the sample. This fact is illustrated in figure 6, in which the plots show the calculated CT density as a function of the height in the sand body for two different images.

3. Evaluation of test results

(*a*) *Stationary states*

First we establish an empirical relationship between the fluid discharge, q, and the hydraulic gradient, J,

$$J = \frac{\mathrm{d}\Phi}{\mathrm{d}z}, \tag{3.1}$$

where Φ is the hydraulic head,

$$\Phi = \frac{p_\mathrm{w}}{\rho_\mathrm{w} g} + z. \tag{3.2}$$

In the above expression, z is the vertical coordinate, p_w and ρ_w are the water pressure and water density, respectively, and g is the acceleration due to gravity. We recall that the critical hydraulic gradient for the 'quicksand' condition is given above by equation (1.1), with $\rho_\mathrm{s} = 2.65\ \mathrm{g\ cm^{-3}}$ as the density of the solids. The porosity in the considered tests varied between 0.35 and 0.40, and with that, the critical hydraulic gradient is estimated to vary between 0.9 and 1.0. As can be seen from figure 7, experimental results are fitted best by Forchheimer's law

$$J = \frac{1}{k_1}\left(1 + \frac{1}{k_2} q\right) q, \tag{3.3}$$

with $k_1 = 4.76\ \mathrm{mm\ s^{-1}}$ and $k_2 = 0.005\ \mathrm{mm\ s^{-1}}$.

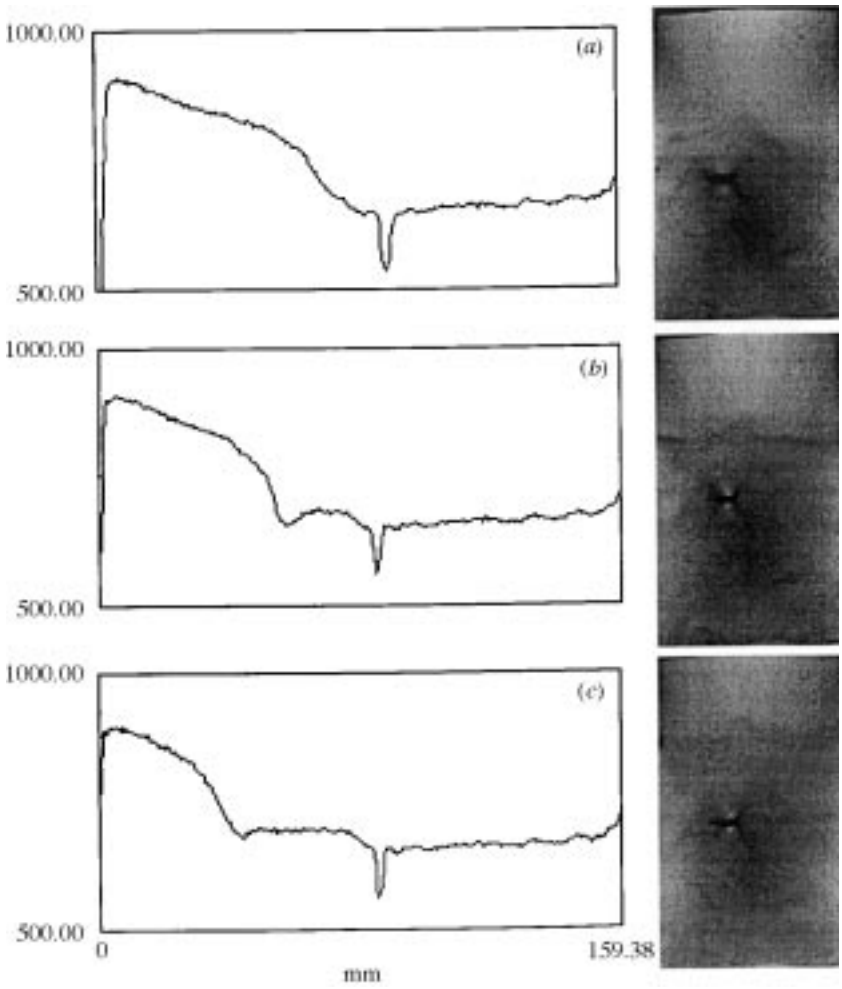

Figure 5. Density variations along the sand body. (*a*) Time 1; (*b*) time 2; (*c*) time 3.

However, the above empirical relationship is not physically meaningful, since, as is well known, the hydraulic resistivities $(1/k_1)$ and $(1/k_2)$ are not constants but functions of porosity and grain size. This defect of the empirical polynomial equation (3.3) with constant coefficients, can be remedied if we look more closely at the experimental results pertaining to the transient phases of the tests.

(*b*) *Transient phases*

Following the above CT observations, we consider a simple wave model for the porosity change due to sudden changes in flow conditions. In that sense, we assume that at the instant of sudden application of any new level of flow rate, a planar porosity wave moves upwards with a speed C, as shown in figure 8. In a first approximation, we assume that the wave-propagation velocity is constant during a transient event, and that the wave front is sharp. This means that for the evaluation of the

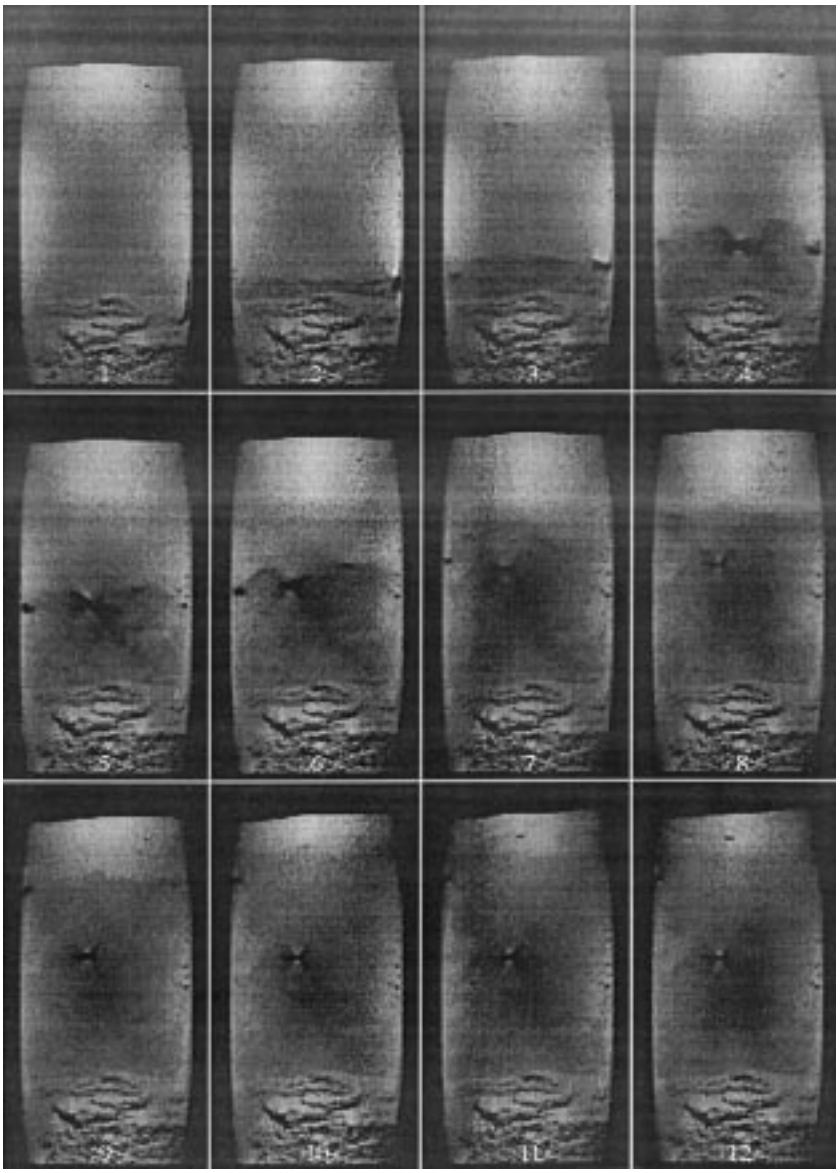

Figure 6. X-ray tomography images from fluidized-column experiments, illustration of the density wave.

test results, we replace the true wave-propagation velocity with its time average,

$$C \approx \bar{C} = \frac{1}{t_1} \int_0^{t_1} C(t)\,\mathrm{d}t. \tag{3.4}$$

The wave-propagation velocity, C, can be computed from the test results as follows: at any state of a transient phase, the average porosity is

$$\bar{\phi} = \phi^- \frac{\bar{C}t}{H_t} + \phi^+ \left(1 - \frac{\bar{C}t}{H_t}\right). \tag{3.5}$$

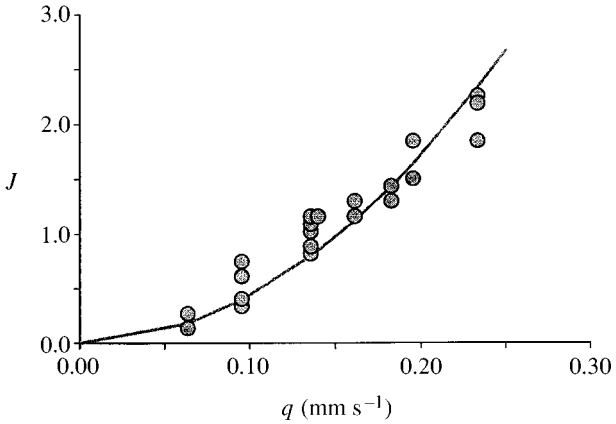

Figure 7. Forchheimer's law as best fit of test 04.

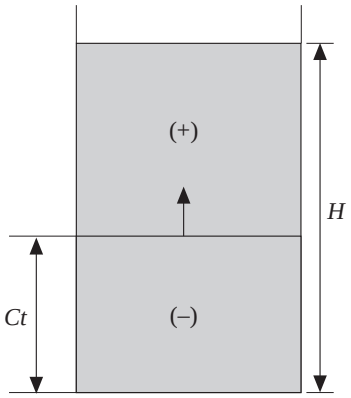

Figure 8. Planar porosity wave moving upwards with speed C.

In this expression, ϕ^+ and ϕ^- are the values of the porosity ahead and behind the wave front, respectively, and H_t is the column height at time t. This average porosity, however, can be directly computed from the measured height, H_t, of the bucket at any instant t:

$$\bar{\phi} = \frac{V_\mathrm{v}}{V} = 1 - \frac{V_\mathrm{s}}{V} = 1 - (1 - \phi_0)\frac{H_0}{H_t}, \tag{3.6}$$

where H_0 and ϕ_0 are initial reference values. Figure 9 shows the practically linear dependency of the average porosity on time in the transient regime for Danish sand, test 06. The drop after a typical travel time,

$$t_\mathrm{t} = H_t/\bar{C}, \tag{3.7}$$

indicates that the forward rarefaction wave has reached the top, and, most probably, a reflected densification wave is moving downwards, leading to some overall compaction. These observations are typical also for the rest of the tests, and indicate that the wave-propagation velocity is practically constant during a particular rarefaction wave event.

The test results shown in figure 9 correspond to an average wave-propagation velocity $\bar{C} = 0.9\,\mathrm{mm\,s^{-1}}$. We remark that in test 06, the fluid discharge was $q =$

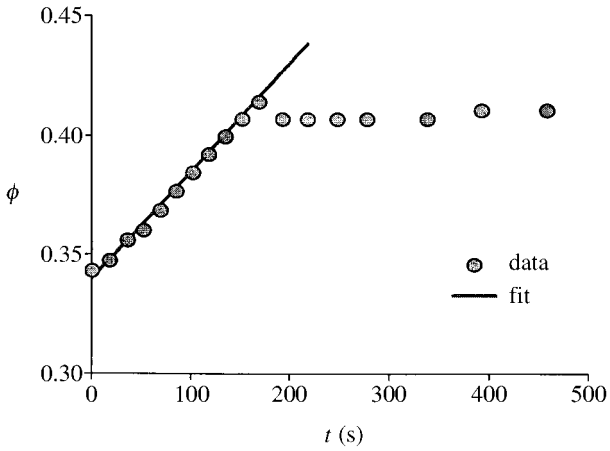

Figure 9. Linear dependency of average porosity on time for test 06, resulting in $C = 0.9$ mm s^{-1}.

0.3 mm s^{-1}, whereas the average porosity varied between 0.34 and 0.41. This means that the corresponding average fluid velocity at the beginning and at the end of the transient phase varied between 0.8 and 0.7 mm s^{-1}. In other words, the porosity wave seems to propagate with a speed which is faster than the fluid average velocity at the beginning and the end of the transient phase by 20–50%. This result was confirmed by test 04 on the Valøygrind sand. The evaluation of the time-average wave-propagation velocity introduced above for the various stages of test 04, is shown in figure 10*a–d*.

4. Theoretical considerations

(*a*) *Permeability modelling*

In a medium with variable density, mass balance is expressed by a storage equation of the general form: 'Inflow' − 'Outflow' = 'Storage' (see figure 11), or more formally by the volume balance equation

$$\mathrm{d}V_{\mathrm{in}} - \mathrm{d}V_{\mathrm{out}} = \Delta \mathrm{d}V_{\mathrm{w}}. \tag{4.1}$$

For a cross-sectional area A, of the sand–water column and no grain transport, the volume balance equation above becomes

$$\left.\begin{aligned} \mathrm{d}V_{\mathrm{in}} = Aq\,\mathrm{d}t, \qquad \mathrm{d}V_{\mathrm{out}} = A\left(q + \frac{\partial q}{\partial z}\,\mathrm{d}z\right), \\ \Delta \mathrm{d}V_{\mathrm{w}} = \mathrm{d}V_{\mathrm{s}}\,\mathrm{d}e = (1-\phi)A\,\mathrm{d}z\frac{1}{(1-\phi)^2}\frac{\partial \phi}{\partial t}\,\mathrm{d}t, \end{aligned}\right\} \tag{4.2}$$

where e denotes the so-called void ratio, and the subscripts 'w' and 's' stand for water-phase and solid-phase, respectively. Equation (4.1) with (4.2) yields, finally, the well-known storage equation (cf. Vardoulakis & Sulem 1995):

$$\frac{\partial \phi}{\partial t} + (1-\phi)\frac{\partial q}{\partial z} = 0. \tag{4.3}$$

If we assume that there is a dependency of q on ϕ, of the form

$$q = Q(\phi), \tag{4.4}$$

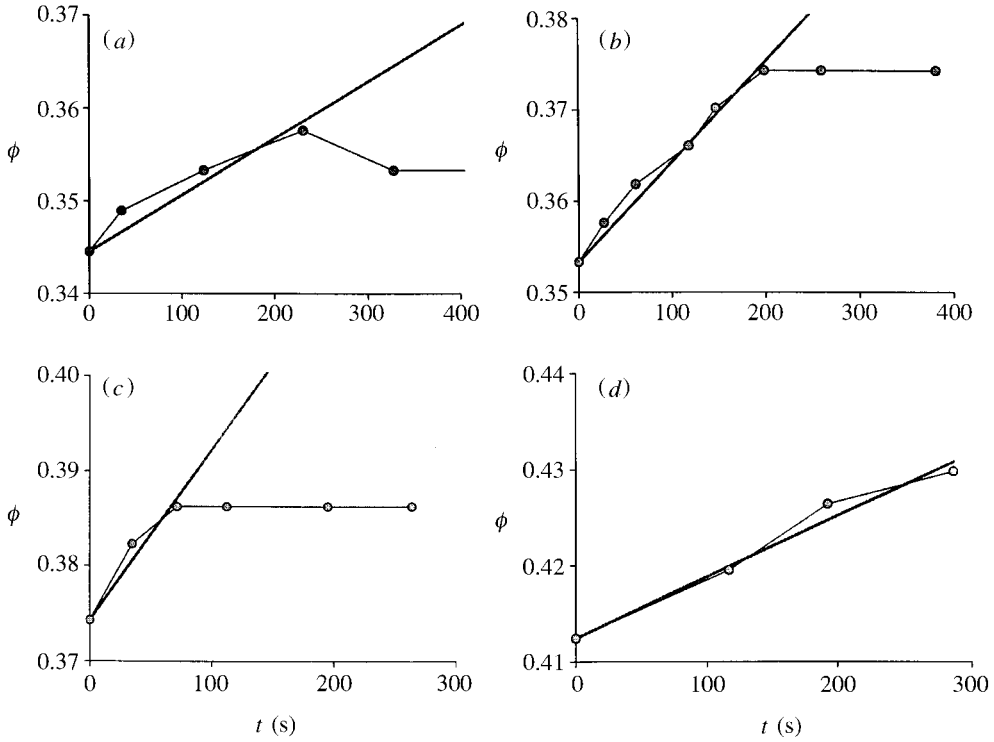

Figure 10. (*a*), (*b*) Wave-propagation velocity for test 04. (*c*), (*d*) Wave-propagation velocity for test 04.

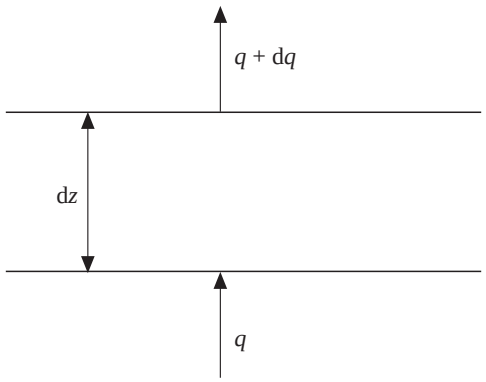

Figure 11. On the storage equation in a two-phase medium.

then equation (4.3) becomes a unidirectional wave equation for forward-travelling porosity waves:

$$\frac{\partial \phi}{\partial t} + C\frac{\partial \phi}{\partial z} = 0, \tag{4.5}$$

with propagation velocity

$$C = (1-\phi)\frac{\mathrm{d}q}{\mathrm{d}\phi}. \tag{4.6}$$

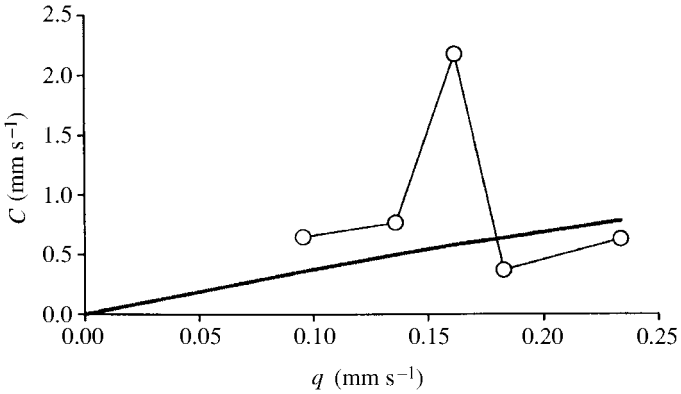

Figure 12. Wave-propagation velocity as a function of fluid-discharge velocity.

We assume that the experimental results presented above are satisfactorily described by setting a linear dependency of the propagation velocity, C, on the discharge, q, of the form

$$C = \lambda(1-\phi)q. \tag{4.7}$$

With $\lambda \approx 6$, the quality of this assumption in relation to the experimental results from test 04 is depicted in figure 12.

(*b*) *Backanalysis of constant-flow-rate tests*

For constant-flow-rate tests (q = const.), the wave-propagation velocity is a decreasing function of porosity, $C = \lambda q(1-\phi)$, and the governing equation becomes

$$\frac{\partial \phi}{\partial t} + \lambda q(1-\phi)\frac{\partial \phi}{\partial z} = 0. \tag{4.8}$$

The characteristics of the wave equation,

$$\frac{\mathrm{d}z}{\mathrm{d}t} = C(\phi), \tag{4.9}$$

are straight lines, whose slopes depend on the initial data. As already mentioned, for not extremely rarefied mixtures, C is increasing with ϕ. Thus, for a rarefaction wave, the characteristics look like the ones sketched in figure 13. This means that in the considered case, any initial anomaly in ϕ, decreasing with z, will become steeper as time progresses. It is thus theoretically possible that for long columns, shocks may develop. The backanalysis of test 04 was done with a simple triangular porosity profile (see figure 14).

Equation (4.8), which is a partial differential equation of hyperbolic type, was solved by using the method of characteristics. Suppose that ϕ is given on the non-characteristic initial curve Γ (e.g. $t = 0$), and let Q be any fixed point on Γ and (C_Q) be the characteristic passing through Q. Along (C_Q) we have

$$\mathrm{d}z - C_J(1-\phi)\mathrm{e}^{-\lambda\phi}\,\mathrm{d}t = 0, \qquad \mathrm{d}\phi = 0. \tag{4.10}$$

Approximating $\mathrm{d}z$, $\mathrm{d}t$ and $\mathrm{d}\phi$ by $z(P) - z(Q)$, $t(P) - t(Q)$ and $\phi(P) - \phi(Q)$, we obtain a pair of algebraic equations which determine the other coordinates of P and the value of ϕ at P.

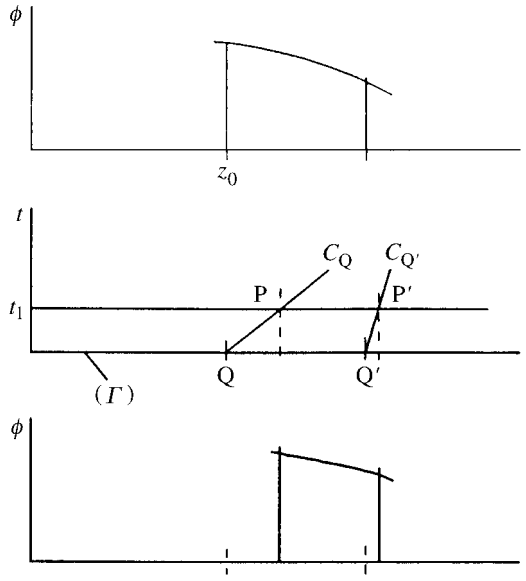

Figure 13. Rarefaction waves tend to break.

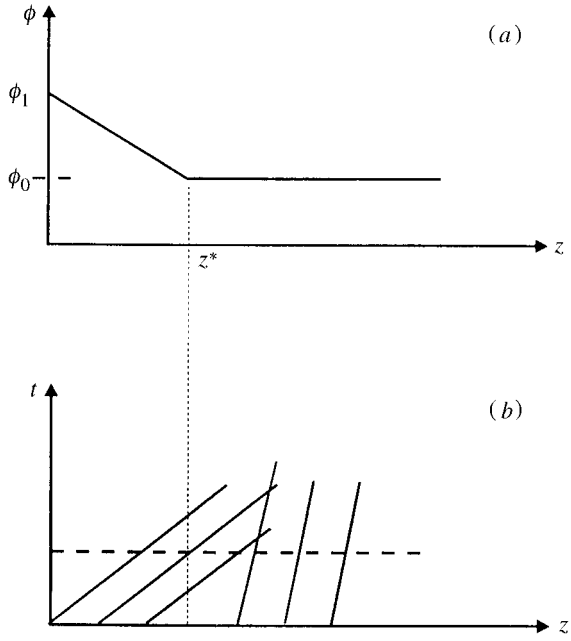

Figure 14. (a) Initial data; (b) characteristic lines.

For the backanalysis of the column test with Valøygrind sand (test 04), where the flow rate was increased, the following parameters were used: initial porosity, $\phi_0 = 0.34$; $\lambda = 6$; and piecewise constant specimen length. Figure 15 shows the motion of the porosity wave. When the porosity wave reaches the top of the sand body (free surface) the system tends to attain equilibrium. By using the value of ϕ

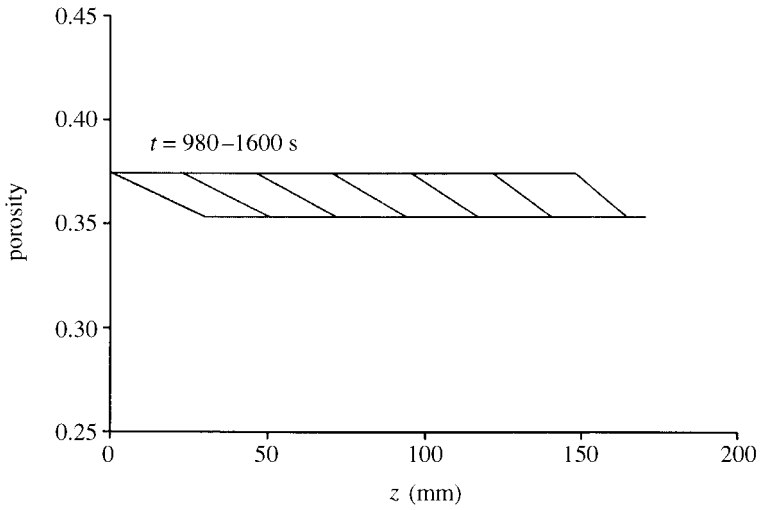

Figure 15. Spatial profiles of porosity at various time-steps (Valøygrind sand, $\lambda = 6$).

at every point and time-step, the density of solids was computed to be

$$\rho' = (1 - \phi)\rho_s, \tag{4.11}$$

in order to comply with the experimental data from CT-scanner imaging and from the measured average values at every time-step. The numerical results for the average porosity, $\bar{\phi} = \bar{\phi}(t)$, and the average density, $\bar{\rho} = \bar{\rho}(t)$, compare satisfactorily in figures 16 and 17.

(*c*) *Permeability functions*

Equations (4.6) and (4.7) lead, formally, to the following expression:

$$\frac{\mathrm{d}q}{\mathrm{d}\phi} = \lambda q. \tag{4.12}$$

The assumed dependency, $q = Q(\phi)$, stems from the fluid-flow law through the dependency of the permeabilities on porosity. In the case of a polynomial law, we have

$$J = a(\phi)q + b(\phi)q^2 = \frac{q}{k_1(\phi)}\left(1 + \frac{q}{k_2(\phi)}\right). \tag{4.13}$$

For constant hydraulic gradient tests ($J = \text{const.} \Rightarrow \mathrm{d}J = 0$) and $q = Q(\phi)$, we get, from equation (4.13),

$$\frac{\partial J}{\partial \phi}\,\mathrm{d}\phi + \frac{\partial J}{\partial q}\,\mathrm{d}q = 0 \quad \Rightarrow \quad \frac{\mathrm{d}a}{\mathrm{d}\phi}q + \frac{\mathrm{d}b}{\mathrm{d}\phi}q^2 + (a + 2bq)\frac{\mathrm{d}q}{\mathrm{d}\phi} = 0.$$

As a result of equation (4.12), the above equation results in

$$\left.\begin{aligned} &\frac{\mathrm{d}a}{\mathrm{d}\phi}q + \frac{\mathrm{d}b}{\mathrm{d}\phi}q^2 + (a + 2bq)\lambda q = 0 \quad \Rightarrow \\ &\qquad \frac{\mathrm{d}a}{a} = -\lambda\,\mathrm{d}\phi \quad \Rightarrow \quad a = a_0 \exp(-\lambda\phi), \\ &\qquad \frac{\mathrm{d}b}{b} = -2\lambda\,\mathrm{d}\phi \quad \Rightarrow \quad b = b_0 \exp(-2\lambda\phi). \end{aligned}\right\} \tag{4.14}$$

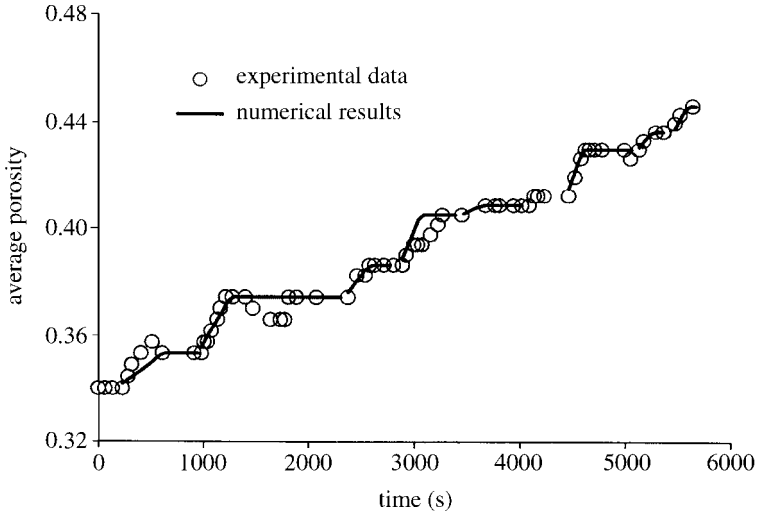

Figure 16. Time evolution of average porosity (Valøygrind sand, $\lambda = 6$).

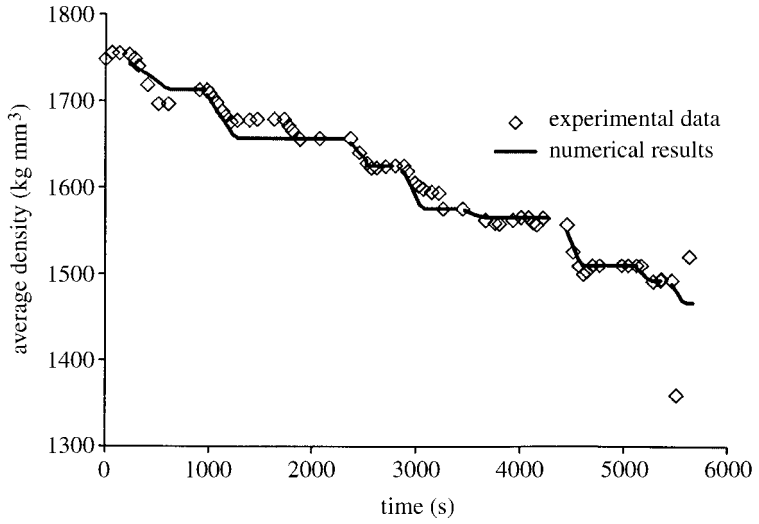

Figure 17. Time evolution of average density (Valøygrind sand, $\lambda = 6$).

This means that the assumed simple wave-speed law, equation (4.7), in conjunction with Forchheimer's polynomial law (4.13), results in complete determination of the hydraulic resistivities a and b as functions of porosity, with only two constants as free parameters. This procedure leads to the following permeability functions:

$$\left.\begin{aligned} k_1 &= k_{10}\exp(\lambda(\phi-\phi_0)) \approx k_{10}(1+\lambda(\phi-\phi_0)+\cdots), \qquad k_{10} = \frac{\mathrm{e}^{\lambda\phi_0}}{a_0}, \\ k_2 &= k_{20}\exp(\lambda(\phi-\phi_0)) \approx k_{20}(1+\lambda(\phi-\phi_0)+\cdots), \qquad k_{20} = \frac{k_{10}}{b_0}. \end{aligned}\right\} \tag{4.15}$$

Figure 18 shows the fit of the flow measurements on the basis of equations (4.13)

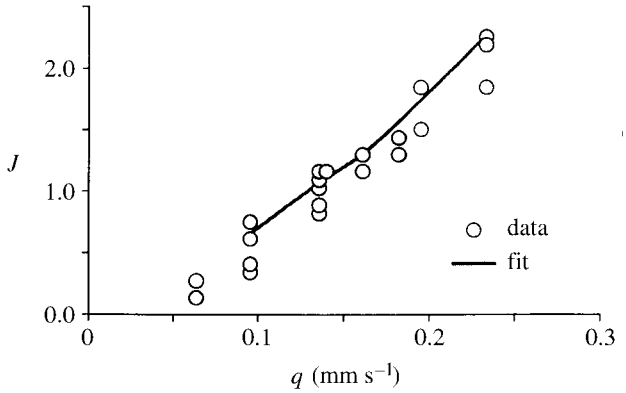

Figure 18. Experimental results and theoretical predictions based on equations (4.12) and (4.13).

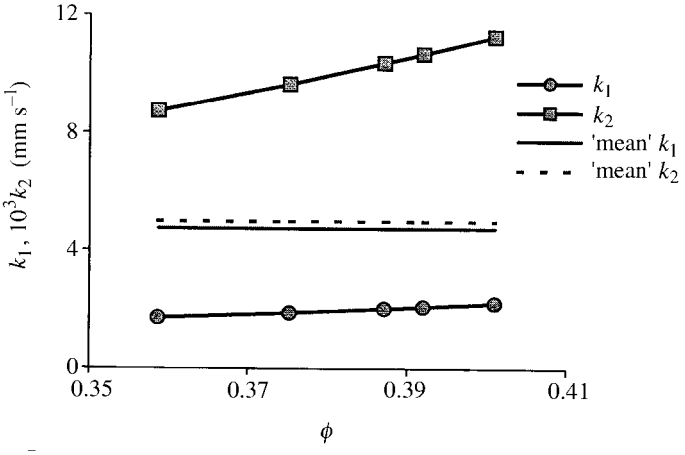

Figure 19. Test 04, dependency of permeabilities k_1 and k_2 on porosity.

and (4.14), and for $k_{10} = 1.54\,\mathrm{mm\,s^{-1}}$ and $k_{20} = 0.00785\,\mathrm{mm\,s^{-1}}$ (with $a_0 = 5$, $b_0 = 4900$ and $\phi_0 = 0.34$). Notice that the fit is passing through the stationary points of each transient phase. The corresponding permeability functions are plotted in figure 19. We observe that the permeability, k_2, is, by three orders of magnitude, smaller than k_1.

For comparison purposes, we recall finally, that in laminar flow for solid sand, the Carman–Kozeny equation calls for a nonlinear dependency of the permeability k_1 on ϕ, i.e.

$$k_{1,\mathrm{lam}} = k_0 \frac{\phi^3}{(1-\phi)^2}. \tag{4.16}$$

This in turn, means that the resistance to flow as described by the hydraulic resistivity, $a = 1/k$, is, in the case of quicksand, much higher than the one for solid sand, as shown in figure 20.

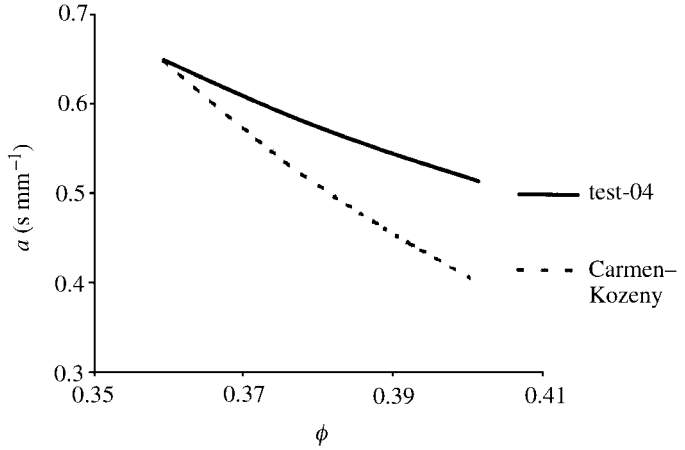

Figure 20. Hydraulic resistivity, $a = 1/k$: (a) quicksand; (b) solid sand.

(d) *Kinematic porosity waves*

For constant hydraulic gradient ($J = \text{const.}$), the quasi-linear wave equation (4.5),

$$\frac{\partial \phi}{\partial t} + C(\phi)\frac{\partial \phi}{\partial z} = 0, \tag{4.17}$$

describes purely *kinematic waves* for the porosity. In this case, the dependency of the wave speed on porosity can be computed explicitly from equation (4.7) with q from equations (4.13) and (4.14),

$$C = \lambda(1-\phi)q, \qquad J = a_0 \mathrm{e}^{-\lambda\phi} q + b_0 \mathrm{e}^{-2\lambda\phi} q^2, \tag{4.18}$$

yielding to

$$C = C_J(1-\phi)\mathrm{e}^{-\lambda\phi}, \qquad C_J = \lambda\frac{a_0}{2b_0}\left(\sqrt{1+4\frac{b_0}{a_0^2}J}-1\right) \approx \lambda\sqrt{\frac{J}{b_0}}. \tag{4.19}$$

The above expression for the propagation velocity of the kinematic wave can be non-dimensionalized by using the kinematic viscosity of water, $\eta_{\mathrm{k}} = 1\ \mathrm{mm}^2\ \mathrm{s}^{-1}$, and the mean grain diameter of the sand,

$$C \approx c\frac{\eta_{\mathrm{k}}}{D_{50\%}}\lambda\sqrt{J}(1-\phi)\exp(\lambda(\phi-\phi^*)), \tag{4.20}$$

where $c = 12.72$ is an empirical constant and $D_{50\%} = 0.15$ mm. In the above expression,

$$\phi^* = 1 - \frac{1}{\lambda} \tag{4.21}$$

is a characteristic value of the porosity of the mixture at which the maximum wave speed is predicted to be

$$C_{\max} = c\frac{\eta_{\mathrm{k}}}{D_{50\%}}\sqrt{J}. \tag{4.22}$$

The experimental results correspond to waves in the ascending branch of the above curve. In figures 12 and 21, we also observe that there is a datum corresponding

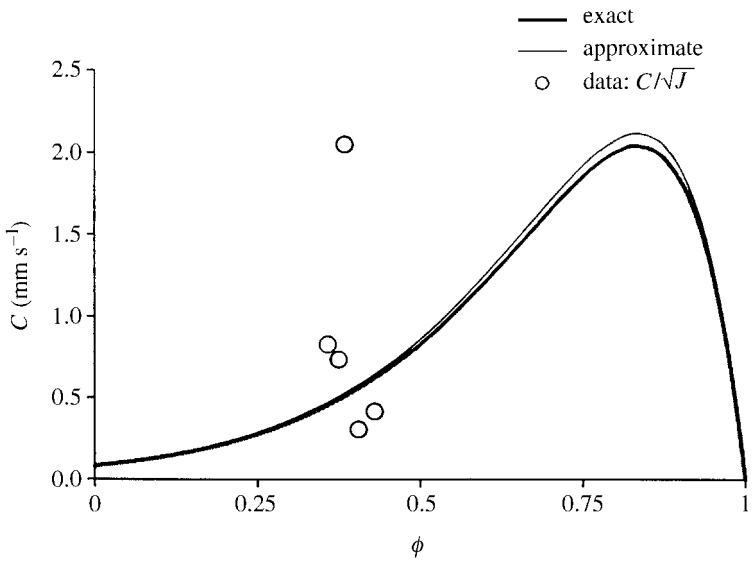

Figure 21. Porosity wave speed as function of porosity ($J = 1$).

most probably to some instability that has resulted in a wave speed very close to the theoretical maximum value. This observation leads to the above, which was computed from overall measurements. A similar result, matching qualitatively the behaviour of the above (C, ϕ)-curve around its maximum, was reported by Harris & Crighton (1994), in conjunction with solitary waves in gas-fluidized beds. Indeed, if one interprets C as a group velocity, then, following standard procedure (Habermann 1998), one can show that at peak ($C = C_{\max}$), solitary waves for the wave amplitude may be predicted which obey the linearized Korteweg–de Vries equation. This in turn may explain the isolated datum in figure 21 (cf. also figure 12).

5. Concluding remarks

Fluidized sand behaves more like a 'compressible' fluid, i.e. a fluid with variable density. Changes in density are due to changes in porosity, i.e. to the concentration of grains per unit volume of the solids–fluid mixture. For the considered fluidized-column test, vertical flow, as described by the flow rate q, is related to the hydraulic gradient, J, through a nonlinear relationship of the form

$$J = J(\phi, q). \tag{5.1}$$

This means that changes in q cause changes in ϕ. The mechanism for the adjustment of porosity to the applied flow rate is a propagating rarefaction wave which obeys a wave equation, i.e. expressing mass balance (storage equation). The density or porosity waves in quicksand propagate with a speed that is proportional to the flow rate and to the solids fraction,

$$C = \lambda(1 - \phi)q. \tag{5.2}$$

In this paper we have demonstrated that the constitutive laws, (5.1) and (5.2), cannot be taken independently. Compatibility of these assumptions results in determination

of the hydraulic resistivity functions, as given above by equations (4.14). Finally, we should remark that the present wave model describes the experimental results quite satisfactorily in the steady as well as in the transient regimes.

We thank Norsk Hydro ASA, and Statoil for permission to publish the results. We also thank Steinar Ommedal Sintef Unimed for operating the X-ray CT-scanner.

References

Forchheimer, P. 1914 *Hydraulik*. Teybner.

Habermann, R. 1998 *Elementary applied partial differential equations*. Prentice-Hall.

Harris, S. E. & Crighton, D. G. 1994 Solitons, solitary waves, and voidage disturbances in gas-fluidized beds. *J. Fluid Mech.* **266**, 243–276.

Irmay, S. 1958 On the theoretical derivation of Darcy and Forchheimer formulas. *Trans. Am. Geophys. Union* **39**, 702–707.

Kenney, T. C. & Lau, D. 1985 Internal stability of granular filters. *Can. Geotech. J.* **22**, 215–225.

Kolymbas, D. 1982 Dynamic compaction of saturated granular media. *Mech. Res. Commun.* **9**, 351–358.

Kolymbas, D. 1994 Compaction waves as phase transitions. *Acta Mechanica* **107**, 171–181.

Scott, R. F. 1986*a* Soil properties from centrifuge liquefaction tests. *Mech. Mater.* **5**, 199–205.

Scott, R. F. 1986*b* Solidification and consolidation of a liquefied sand column. *Soils Found.* **26**, 23–31.

Skempton, A. W. & Brogan, J. M. 1994 Experiments on piping in sandy gravels. *Géotechnique* **44**, 449–460.

Skjaerstein, A., Stavropoulou, M., Vardoulakis, I. & Tronvoll, J. 1997 Hydrodynamic erosion: mechanism of sand production in weak sandstones. *Int. J. Rock Mech. Mining Sci.* **34**, 3–4.

Stavropoulou, M. 1996 Coupled hydromechanical instabilities in deep boreholes. PhD thesis, National Technical University of Athens, Greece.

Taylor, D. W. 1948 *Fundamentals of soil mechanics*. New York and London: Wiley.

Vardoulakis, I. & Sulem, J. 1995 *Bifurcation analysis in geomechanics*, § 5.6.3. Blackie.

Vardoulakis, I., Stavropoulou, M. & Papanastasiou, P. 1996 Hydromechanical aspects of sand production problem. *Transport in Porous Media* **22**, 225–244.

PHILOSOPHICAL TRANSACTIONS OF THE ROYAL SOCIETY A MATHEMATICAL, PHYSICAL & ENGINEERING SCIENCES